EFFECTS OF FORMING SPECIFIC PRESSURE AND FILLING SPEED ON MICROSTRUCTURE AND MECHANICAL PROPERTIES OF THIN-WALLED CuSn10P1 ALLOY PARTS BY RHEOLOGICAL SQUEEZE FORMING

Wentao Xiong, Zhangxing Liu, Ke Wen and Xinhua Yin
Faculty of Materials Science and Engineering, Kunming University of Science and Technology, Kunming 650093, People's Republic of China

Rongfeng Zhou and Yongkun Li
Faculty of Materials Science and Engineering, Kunming University of Science and Technology, Kunming 650093, People's Republic of China
City College, Kunming University of Science and Technology, Kunming 650051, People's Republic of China

Abstract

Semi-solid rheological squeeze forming has distinct advantages over traditional casting and forming techniques. In this study, a high-performance thin-walled CuSn10P1 alloy was successfully produced by combining liquid-metal instantaneous undercooling-induced nucleation, semi-solid slurry homogenization treatment, and semi-solid rheological squeeze forming. The effects of the forming specific pressure (MPa) and filling speed (mm/s) on the microstructure and mechanical properties of these parts were explored in this study, and the influence of the intergranular brittle phase (α-Cu + δ-Cu$_{41}$Sn$_{11}$ + Cu$_3$P) content on the mechanical characteristics was determined. CuSn10P1 alloy with a Cu$_{13.7}$Sn phase exhibiting a large number of spherical or nearly spherical morphological features coexisting with the high-tin solid-solution layer morphology was discovered and prepared at a mold temperature of 485 °C, specific pressure of 165 MPa, and filling speed of 22 mm/s. Parts with this microstructure had excellent mechanical properties, including an ultimate tensile strength of 419.95 MPa, yield strength of 228.89 MPa, and an elongation of 13.71%. This study illustrates the viability of semi-solid rheological squeeze casting for manufacturing high-performance thin-walled high-tin copper alloys.

Keywords: CuSn10P1 alloy semi-solid rheological squeeze casting, liquid-metal instantaneous undercooling-induced nucleation, metal semi-solid slurry preparation technology, microstructure, mechanical properties

Introduction

As important alloys for industrial applications,[1] Cu–Sn alloys are widely used in the manufacture of bushings, impellers, and electronic equipment connectors owing to their high strength and toughness, wear resistance, corrosion resistance, and excellent electrical conductivity. They can meet the high-performance requirements of certain components in high-speed railways, aircraft, and ships.[2–5]

Semi-solid processing (SSP) is a metal-forming technique that combines the advantages of traditional forging and casting.[6] Compared to forged products, SSP can produce complex parts with near-net shapes,[7,8] excellent mechanical properties, and good surface quality.[9] Aluminum and magnesium alloys have been extensively studied over a wide range of semi-solid temperatures.[10–13] Apelian et al.[14,15] proposed a continuous rheoconversion process (CRP) based on passive liquid-mixing technology to obtain spherical structures by controlling the nucleation and growth of the primary phase; it is now widely used in aluminum–copper (A206), wrought aluminum, and Mg alloys. However, semi-solid processing is difficult for high-melting point alloys owing to the wide temperature range

of the solid–liquid lines. Nonetheless, the unique semi-solid structures with excellent mechanical properties have attracted research interest.[16] Meng et al.[17,18] demonstrated the feasibility of recrystallization and partial melting (RAP) method for producing semi-solid blanks of SKD61 steel with a homogeneous spherical microstructure. Jiang et al.[19] studied semi-solid blanks in the GH4037 alloy preparation process and investigated their microstructural evolution.

In addition to research on the application of semi-solid forming technology to steel- or nickel-based high-temperature alloys, SSP of copper alloys has been reported. Cao et al.[20] proposed a method for preparation of semi-solid copper alloys by rotary swaging strain-induced melt activation (RSSIMA) and investigated the influence of tissue characteristics on the elastic–plastic properties of semi-solid tin–copper alloys. Jia et al.[21] investigated the effect of semi-solid isothermal treatment on the Cu–10Ni–Si (mass fraction, wt%) alloy and the effect of the solid-solution treatment process on the microstructure and phase composition.

From the analysis, the main research methods for high-melting point alloys are based on thixotropy. It is relatively easy to store and transport blanks using thixotropic technologies. However, the length and complexity of the preparation process for semi-solid paste increase production costs and are not favorable for industrial use. High-melting point alloys are characterized by high forming temperatures, rapid temperature drops, and high requirements for semi-solid slurry preparation, limiting the use and development of rheological forming technologies.[19] Nevertheless, with the great potential of semi-solid rheology,[22] the rheological forming of high-melting point alloys has attracted research attention, particularly in the steel industry.[23] High-tin copper alloys are particularly vulnerable to brittle Cu_x–Sn_{100-x} intermetallic phases such as δ-$Cu_{41}Sn_{11}$ in conventional casting processes, making them unsuitable for plastic processing.[24,25] Thus, high-tin copper alloys are restricted to cast products[26–29] and are unsuitable for technical applications.[5,29] Korean researchers[5,30] investigated the toughening of $CuSn_{22}$ alloy after annealing at 750 °C and deformation at high temperatures. The strengths of air- and water-cooled specimens improved; plasticity increased from 0.2% in the as-cast specimen to 0.3% and 3.6%, respectively, indicating the little possibility of use in plastic processing. When deformed after annealing at temperatures ranging from 320 to 500 °C, tin elements diffused from the intergranular to the intracrystalline; when deformed after annealing at temperatures ranging from 500 to 800 °C, tin elements migrated to the intergranular.[31] Thus, the potential law of the brittle phases and high-tin copper alloy parts must be clarified to reduce or eliminate the high-tin brittle δ-$Cu_{41}Sn_{11}$ phase as much as possible in semi-solid rheological squeeze casting.

This study investigates the effect of different rheological squeeze-forming process parameters on the microstructure and mechanical properties of CuSn10P1 alloy, focusing on the relationship between forming specific pressure (MPa) and filling speed (mm/s) in the intergranular brittle phase (α + δ + Cu_3P). In addition, the microstructural evolution and strengthening mechanism of CuSn10P1 alloy rheological squeeze parts were investigated. The results confirm the feasibility of melt transient undercooling-induced nucleation in production and industrial application of high-performance thin-walled CuSn10P1 alloy parts with high strength and plasticity.

Experimental Procedures

Materials

The experimental material was a CuSn10P1 copper alloy bar (Ø 91 mm). The solid–liquid temperature range of the CuSn10P1 alloy was measured as 185.0 °C (839.3–1024.3 °C) by differential scanning calorimetry (DSC, NETZSCH STA449F3). Fluorescence spectrometry (Axios pw4400 X-ray) was used to determine the sample composition, as shown in Table 1.

Preparation of CuSn10P1 Alloy Semi-solid Slurry and the Rheo-squeeze Casting Process

Figure 1 shows a schematic of the CuSn10P1 alloy semi-solid slurry preparation and rheological squeeze casting, with four processes, as shown in Figure 1a.

(a) Purification and melting processes. As shown in Figure 1b, 5.5 kg ± 50g of CuSn10P1 alloy was melted in a medium-frequency induction furnace; the 1200 ± 1 °C CuSn10P1 melt was purified by degassing and de-slagging, followed by air cooling to 1080 ± 1 °C in the furnace.

(b) CuSn10P1 semi-solid slurry preparation process. As shown in Figure 1c, the self-designed and developed liquid-metal instantaneous undercooling-induced nucleation semi-solid slurry preparation device was used; the device's tilt angle was set at 45°; the real-time flow rates of the upper and lower water tanks were set to 30 ml/s and 25 ml/s, respectively. Liquid-metal instantaneous undercooling-induced nucleation (LMIUIN stage) was performed on the purified CuSn10P1 alloy melt, resulting in a large temperature drop (approximately 90 °C) in a short period of

Table 1. Chemical Composition of CuSn10P1 Alloy

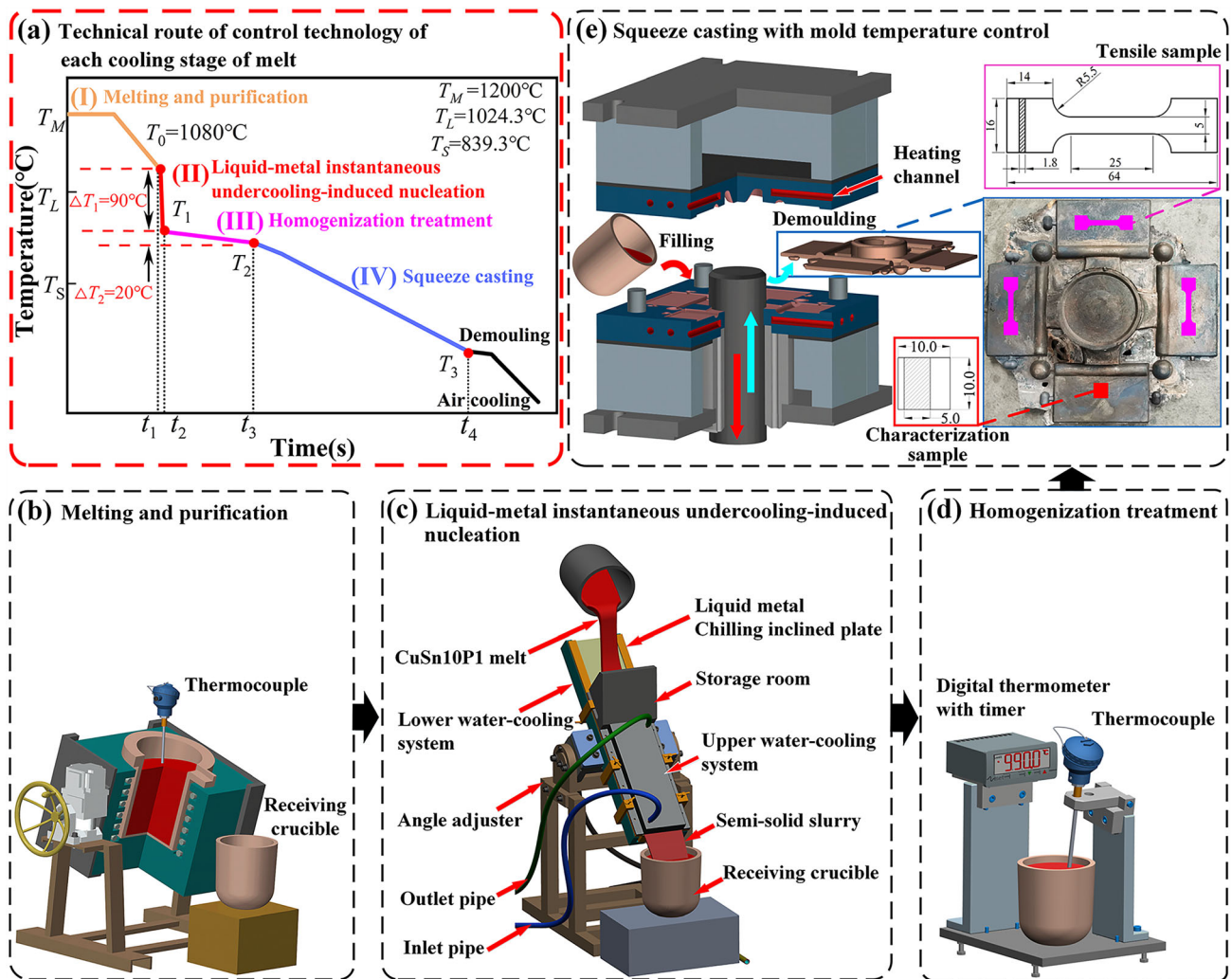| Element	Cu	Sn	P	Impurity
Content [wt%]	88.76	9.89	0.85	0.17

Figure 1. Schematic of semi-solid slurry preparation and rheological squeeze-forming process.

time, resulting in a high cooling rate (approximately 450 °C/s).[32] A graphite crucible with a preheating temperature of 990 °C was used to collect the semi-solid slurry.

(c) Homogenization treatment (HT stage). As shown in Figure 1d, the short-term homogenization treatment (20 ± 1 s) was completed after collection of the CuSn10P1 semi-solid slurry by preheating the crucible at 990 °C.

(d) CuSn10P1 alloy semi-solid rheological squeeze-casting process (SC stage). To complete squeeze forming, the semi-solid slurry of CuSn10P1 alloy in the collected crucible was injected into the bottom injection extruder, maintaining pressure for 20 ± 0.5 s before removal from the mold and air cooling (Figure 1e).

Microstructure and Mechanical Property Analysis

To broaden the application of CuSn10P1 alloy parts, the parts investigated in this study simulated a specific type of marine slide rail sheet with a maximum thickness of 5 mm. The squeezing process parameters were designed according to the orthogonal test design scheme presented in Table 2 to study the influence of different squeeze process parameters on the microstructure and properties of CuSn10P1 alloy parts. The microstructure observation and tensile samples were processed according to their positions and sizes, as shown in Figure 1d. The microstructures of the samples were examined using a Wuxi brand sandpaper; the samples were polished using 280#, 400#, 600#, 800#, and 1000# metallographic sandpapers in turn, before

Table 2. Factors Levels of Orthogonal Test for the Rheo-squeeze Casting Parameters

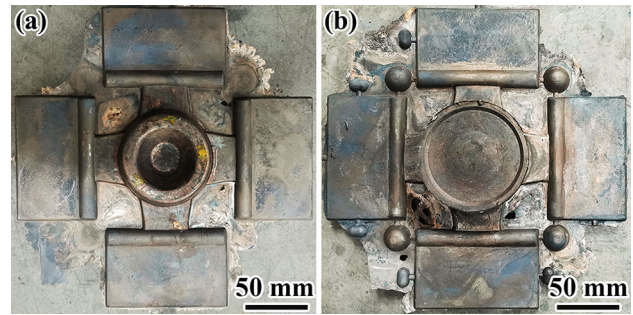| Experimental serial number	Forming specific pressure (MPa)	Filling speed (mm/s)	Mold preheating temperature (°C)
1	145	18	485
2	145	20	485
3	145	22	485
4	155	18	485
5	155	20	485
6	155	22	485
7	165	18	485
8	165	20	485
9	165	22	485

Figure 2. Macrograph of rheo-squeeze CuSn10P1 parts.

The area and perimeter of the solid particles are denoted as A_i and P_i, respectively; the total number of solid particles is denoted as N. If F approaches 1, it suggests that the solid particles are circular.

Result

Macroscopic Morphology of CuSn10P1 Parts

The macroscopic morphology of CuSn10P1 semi-solid rheologically formed parts is depicted in Figure 2. The research object of this study is a thin-walled part composed of a rectangular sheet with a wall thickness of 5 mm. Filling of the parts was complete in all experiments; no cracks appeared, and the parts had good surface quality.

Microstructure and Mechanical Properties of Rheo-squeeze CuSn10P1 Alloy Based on Orthogonal Experimental Design

In this study, $L_9(3)^2$ orthogonal table (Table 3) was created to explore the influence degree and influence law of different factors on the ultimate tensile strength (MPa) and elongation (%) of the CuSn10P1 alloy parts. Each factor had three levels values that all were determined experimentally.

The statistical analysis results for the effects of forming specific pressure (MPa) and filling speed (mm/s) on the ultimate tensile strength (MPa) and elongation (%) are presented in Table 4. Single-factor analysis was performed on the results of the orthogonal experimental design to determine the influence of a single factor on the ultimate tensile strength (MPa) and elongation (%). Furthermore, range analysis (RA) results revealed the most significant factors. K_i ($i = 1, 2, 3$) is the mean of the level values of the factors presented in Table 3. The range (R) is the difference between the maximum and minimum level values, as indicated in Table 4. According to the results of the range analysis provided in Table 4, the order of significant levels for both ultimate tensile strength (MPa) and elongation (%) is represented as: 'filling speed > forming specific

mechanical polishing with a 500 nm diamond polishing liquid. After polishing, the samples were corroded for 7–8 s with a 10% $FeCl_3$ solution (10 mL $FeCl_3$ + 10 mL HCl + 100 mL H_2O), washed with anhydrous ethanol, and dried. The microstructure and fracture morphology of the samples were examined using a Nikon ECLIPSE MA200 metallographic microscope (OM). The microstructures and elemental distributions of the parts were examined using a tungsten-filament scanning electron microscope (FE-SEM) in conjunction with an energy-dispersive spectrometer (EDS). Dog-bone-shaped tensile specimens were tested on a universal testing machine at a tensile speed of 1 mm/min at room temperature. The yield strength (YS), ultimate tensile strength (UTS), and elongation (EL) of the specimens were determined using tensile stress–strain curves. To improve the statistical significance, three replicate tensile tests were performed on the CuSn10P1 parts for all process parameters. The standard deviation was used to measure the extent to which the test results deviated from the arithmetic mean to gauge the validity and accuracy of the data, calculated as

$$S = \sqrt{\frac{\sum_{i=1}^{n}(S_i - \overline{s})^2}{n}} \qquad \text{Eqn. 1}$$

where S is standard deviations; S_i ($i = 1, 2, 3$) is the test result; $\overline{s}$ is the mean of the three test results; and n is the total number of samples.

Image-Pro Plus software was used to quantify the average grain size (D) and shape factor (F), which were determined using Eqs. (2) and (3):[16]

$$D = \frac{\sum_{i=1}^{N}\sqrt{4A_i/\pi}}{N} \qquad \text{Eqn. 2}$$

$$F = \frac{\sum_{i=1}^{N}4\pi A_i/P_i^2}{N} \qquad \text{Eqn. 3}$$

Table 3. Description of Process Parameters in Each Experiment

Experimental serial number	Forming process parameters		Experimental results		
	Forming specific pressure (MPa)	Filling speed forming (mm/s)	Ultimate tensile strength (MPa)	Yield strength (MPa)	Elongation (%)
1	145	18	350.97±4.67	251.97±2.79	5.44±1.29
2	145	20	375.70±2.90	229.23±3.24	8.17±0.59
3	145	22	397.87±4.24	226.76±4.66	13.25±1.14
4	155	18	344.71±12.10	229.74±8.67	5.97±1.57
5	155	20	365.12±8.21	212.86±5.27	8.84±1.47
6	155	22	380.81±11.39	228.77±5.79	10.96±0.82
7	165	18	364.77±8.25	221.68±7.25	8.74±1.40
8	165	20	350.35±15.19	222.82±3.54	5.22±0.74
9	165	22	400.70±13.63	230.53±2.24	13.01±0.88

Table 4. Results of Range Analysis

Factors	Forming specific pressure (MPa)	Filling speed (mm/s)	Forming specific pressure (MPa)	Filling speed (mm/s)
	Ultimate tensile strength (MPa)		Elongation (%)	
K_1	374.85	353.48	8.95	6.72
K_2	363.55	363.72	8.59	7.41
K_3	371.94	393.13	8.99	12.41
R	8.39	29.40	0.40	5.69

Figure 3. Effect of single-factor analysis on mechanical characteristics of CuSn10P1 alloy parts.

pressure,' indicating that the filling speed had a greater impact on the mechanical characteristics than the forming specific pressure.

Figure 3 shows a law graph of the effects of each factor K_i (i = 1, 2, 3) on the ultimate tensile strength (MPa) and elongation (%) based on the results of Table 4. The graph shows that as the forming specific pressure increases from 145 to 165 MPa, the ultimate tensile strength decreased by 3.01% and then increased by 2.31%, with an overall decreasing trend. The effect on elongation decreased and then increased, but the effect on elongation (%) was insignificant. When the forming specific pressure reached 165 MPa, the average elongation was essentially the same as that at 145 MPa. Similarly, when the filling speed increased, the ultimate tensile strength increased slightly (2.90%), and, then increased significantly (8.09%), with a overall increasing trend. Although the ultimate tensile strength and elongation increased at a filling speed of 22 mm/s compared with 18 mm/s and 20 mm/s, respectively, this does not imply that continuing to increase the filling speed improves tensile strength and elongation. Previous research by our research group discovered that at a filling speed of 25 mm/s, the average values of the ultimate tensile strength (MPa) and elongation (%) were 386.40 MPa and 9.07%,[33] respectively, significantly less than the average values of 397.87 MPa and 13.25% in this study.
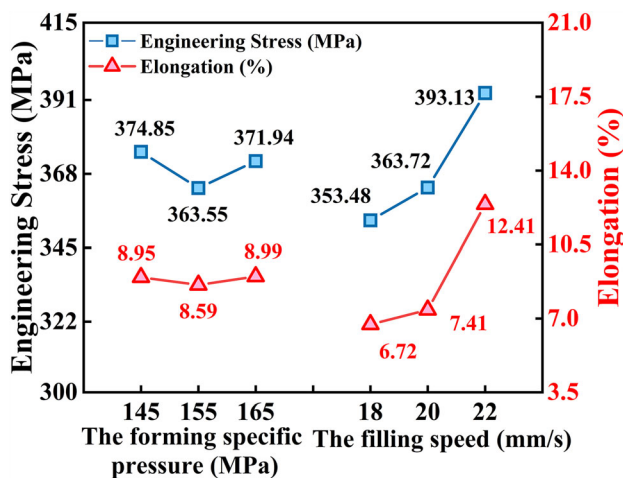
Higher filling speeds (above 25 mm/s) are likely to increase the number of shrinkage holes owing to air entrapment. Cracks tend to sprout at the defects during the loading process, causing the part to fail. In summary, for the best quality and mechanical properties, the best forming process parameters for the parts in this study should be a mold preheating temperature of 485 °C, a forming specific pressure of 145, 165 MPa, and a filling speed of 22 mm/s.
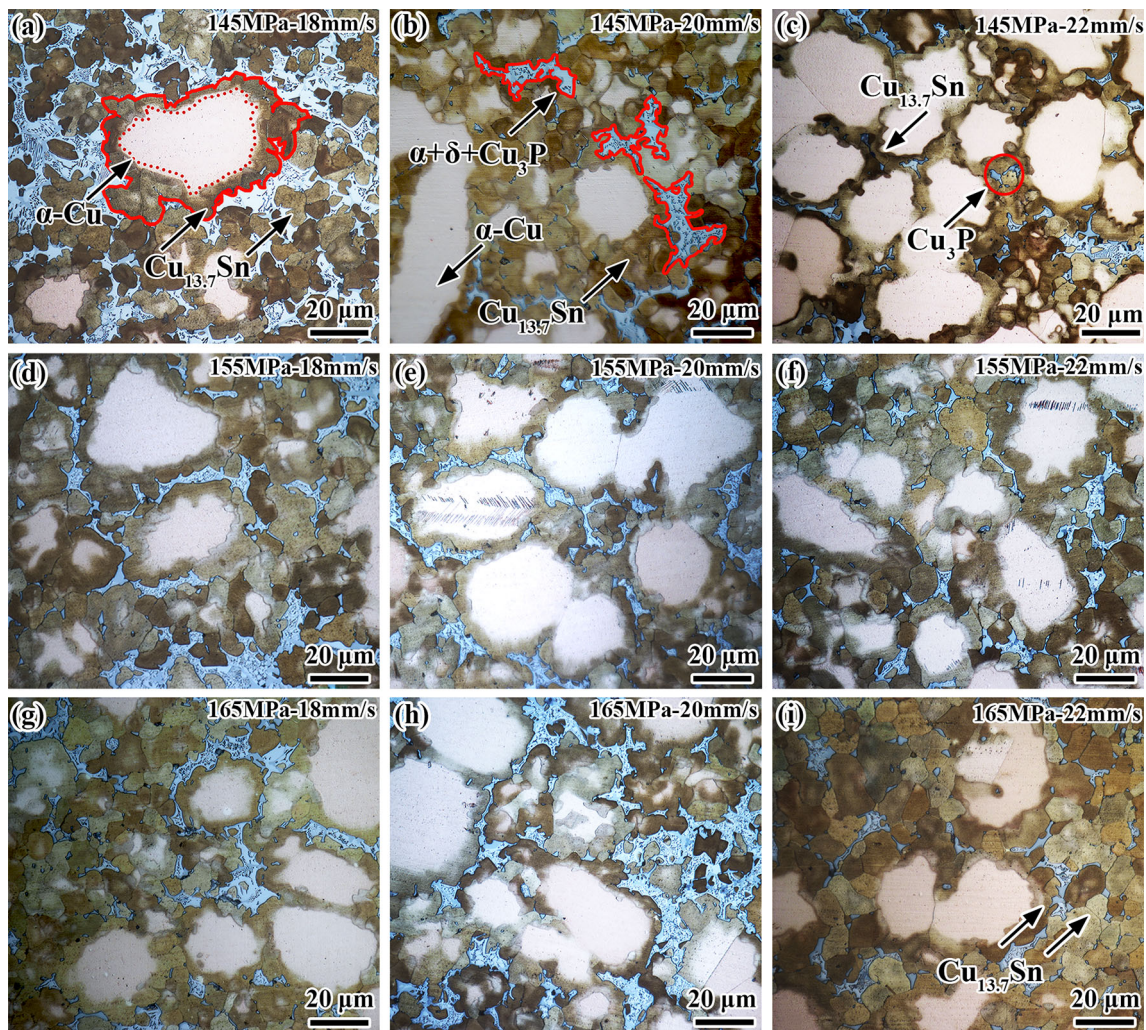
Figure 4. Microstructure of CuSn10P1 alloy semi-solid rheological squeeze parts with different process parameters.

Figure 4 depicts the microstructure of the CuSn10P1 alloy parts with the nine sets of semi-solid rheo-squeeze process parameters, with metallographic photo sequences corresponding to the nine experimental sequences. The microstructural composition is generally consistent with previous research results from our group;[32–36] subsequent XRD and EDS spot-scan results confirm that the part consists of the primary α-Cu phase, the Cu13.7Sn phase, the Cu3P phase, and the δ-Cu41Sn11 phase. The primary α-Cu phase mainly appears as a light-brown spherical or subspherical organization; the $Cu_{13.7}Sn$ phase mainly wraps the primary α-Cu phase in a dark-brown ring-like structure, appearing as a dark-brown spherical or subspherical equiaxed crystal with some process parameters. The δ-$Cu_{41}Sn_{11}$ phase, together with the Cu_3P phase and a small amount of the primary α-Cu phase, forms the intergranular organization (α-Cu + δ-$Cu_{41}Sn_{11}$+Cu_3P), mainly

appearing as light-blue river-like or sheet-like structures surrounding primary α-Cu phases; a similar phenomenon was found by Zhou et al.[32,33,37]

In Figure 4a–i, although the composition of the phases is the same, the shape, distribution, and composition of the intercrystalline phase (α + δ + Cu_3P) are distinct, and can be classified into three categories:

(1) The light-blue intergranular phase content increased, as shown in Figure 4b, e, and g, and the spherical structure formed by the primary α-Cu phase and $Cu_{13.7}Sn$ phase was half-wrapped in a long flake shape.

(2) As shown in Figure 4a, d, and h, the light-blue intercrystalline phase content was substantially enhanced, exhibiting a clear river-like structure
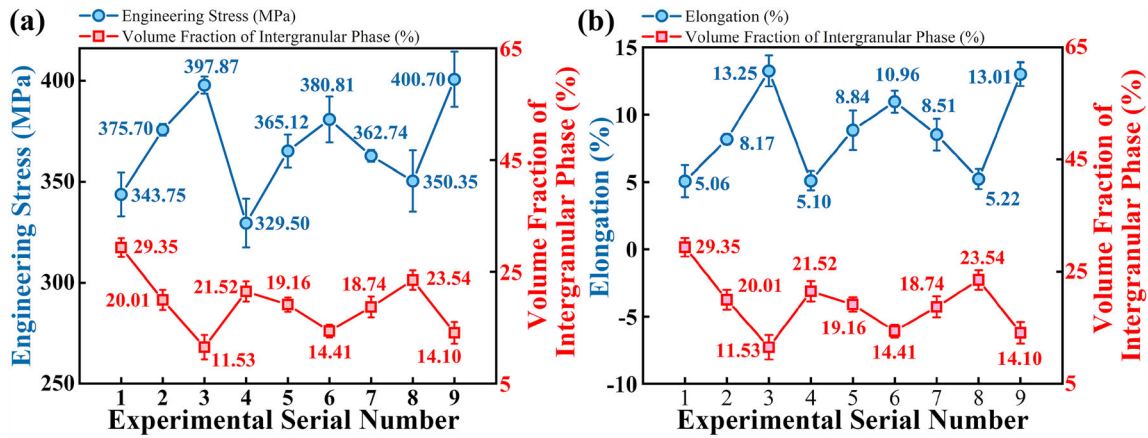
Figure 5. *Relationship between the volume fraction of intergranular phase and (a) ultimate tensile strength; (b) elongation with different process parameters.*

that was highly unevenly distributed around the grains, and isolating them as islands.

(3) As shown in Figure 4c, f, and i, the intercrystalline phase content is the lowest and was only sporadically dispersed throughout the globular microstructure.

The statistics of no less than 20 optical micrographs of the parts produced by each set of nine process parameters were used to create an association between the intergranular brittle phase, ultimate tensile strength (MPa), and elongation (%) (Figure 5). The overall ultimate tensile strength decreased as the percentage of intergranular structures increased, as shown in Figure 5a. When the volume percentage of the intercrystalline phase was increased by 1%, the ultimate tensile strength decreased by 6.35 MPa compared to the highest value of the average ultimate tensile strength (400.70 MPa) of the research object. The maximum decrease in the ultimate tensile strength of high-intercrystalline phase parts relative to low-intergranular content parts was 17.77%; the average decrease was 10.59%. Similarly, as shown in Figure 5b, as the percentage of intergranular structure increased, the elongation decreased, indicating a clear inverse relationship. A 1% increase in the intercrystalline phase reduced the elongation by 0.58%. The maximum reduction in elongation with a high-tin intercrystalline structure was 61.81% compared to parts with a low intercrystalline structure; the average reduction was 38.80%.

As a result, the influence of forming process parameters on the properties of the CuSn10P1 alloy rheological squeeze part was primarily due to the significant influence of the forming process parameters on the content and distribution of the intergranular phase. In conjunction with the results of our previous study,[32] it was discovered that the intercrystalline phase had an unfavorable effect on the comprehensive mechanical characteristics of the parts, with a particularly severe negative effect on their elongation.
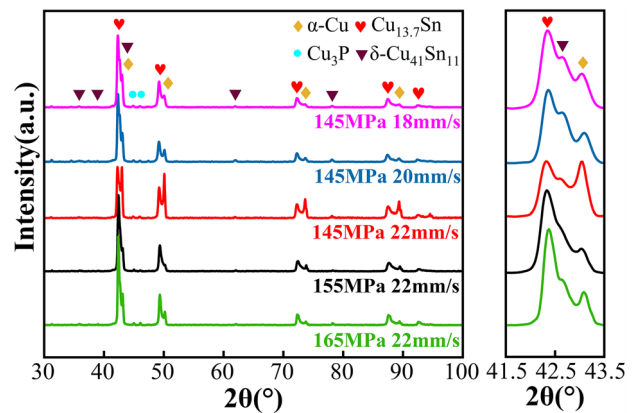

Figure 6. *XRD results with different process parameters.*

Effect of Rheo-squeeze Casting Process Parameters on Microstructure and Mechanical Properties of CuSn10P1 Alloy Parts

Microstructure

With the orthogonal experimental design results, the essence of different mechanical properties of CuSn10P1 alloy semi-solid rheo-squeezed parts is attributed to different contents of the intergranular phase ($\alpha + \delta + Cu_3P$) caused by different forming parameters. Furthermore, the $Cu_{13.7}Sn$ phase exhibited distinct microstructures with specific sets of process parameters. Therefore, the relationship between the microstructure and mechanical properties of the CuSn10P1 alloy parts No. 1, 2, 3, 6, and 9 in Table 4 was analyzed using the control variable method to more regularly investigate the influence of the microstructure of the intercrystalline phase on the mechanical properties of the parts with different parameters.

Figure 6 shows the XRD patterns of the parts with different process conditions. Figure 7 shows the SEM morphology,
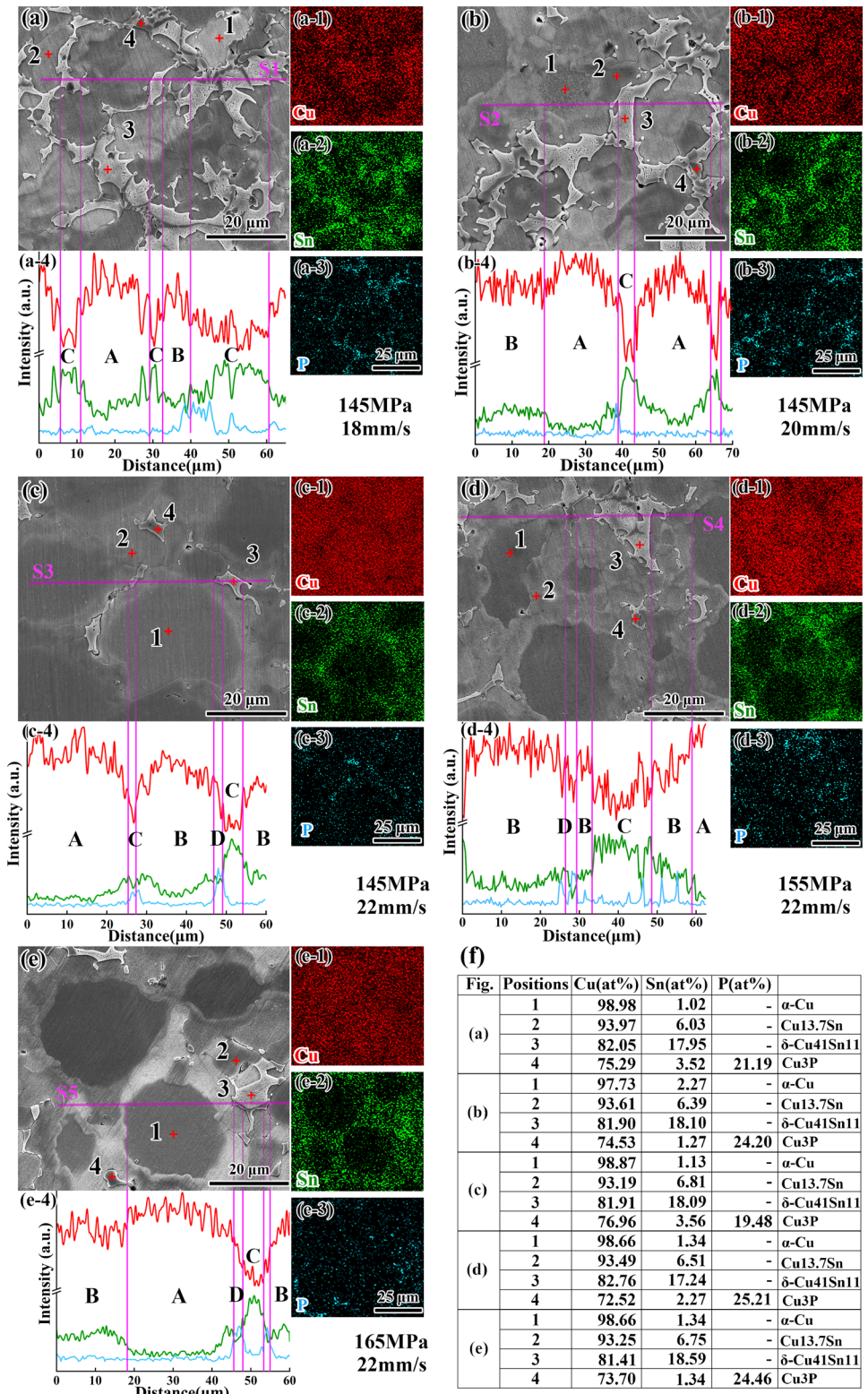
Figure 7. SEM images of CuSn10P1 alloy parts with different process parameters (a)–(e), EDS element distribution mapping (a-1)–(a-3), (b-1)–(b-3), (c-1)–(c-3), (d-1)–(d-3), (e-1)–(e-3), EDS line-scan results (a-4)–(e-4), (f) summarizes the point analysis results.

Fig.	Positions	Cu(at%)	Sn(at%)	P(at%)	
(a)	1	98.98	1.02	-	α-Cu
	2	93.97	6.03	-	Cu13.7Sn
	3	82.05	17.95	-	δ-Cu41Sn11
	4	75.29	3.52	21.19	Cu3P
(b)	1	97.73	2.27	-	α-Cu
	2	93.61	6.39	-	Cu13.7Sn
	3	81.90	18.10	-	δ-Cu41Sn11
	4	74.53	1.27	24.20	Cu3P
(c)	1	98.87	1.13	-	α-Cu
	2	93.19	6.81	-	Cu13.7Sn
	3	81.91	18.09	-	δ-Cu41Sn11
	4	76.96	3.56	19.48	Cu3P
(d)	1	98.66	1.34	-	α-Cu
	2	93.49	6.51	-	Cu13.7Sn
	3	82.76	17.24	-	δ-Cu41Sn11
	4	72.52	2.27	25.21	Cu3P
(e)	1	98.66	1.34	-	α-Cu
	2	93.25	6.75	-	Cu13.7Sn
	3	81.41	18.59	-	δ-Cu41Sn11
	4	73.70	1.34	24.46	Cu3P

line-scanning energy spectrum, and surface-scanning energy spectrum of the parts. Figure 7f shows the scanning findings for each point in Figure 7a–e. Combining the standard PDF cards and the aforementioned metallographic morphological characteristics (Figure 4), it is observed in Figure 6 and Figure 7a–f that the microstructure of the parts with different process settings is constituted of four phases: (1) a low-Sn primary α-Cu phase (1-point region) with a gray, spherical or near-spherical form with an Sn concentration of 1.02–2.27 at%; (2) high-tin $Cu_{13.7}Sn$ phases that appear light gray and wrap the primary α-Cu phase in a ring form, or in a separate spherical or sub-spherical phase aggregated outside the primary α-Cu phase, and with an Sn content of 6.03–6.81 at% and a Cu:Sn atomic ratio of 13.7:1 (2-point region); (3) the δ-$Cu_{41}Sn_{11}$ phase is off-white and connected in sheets with a Cu:Sn atomic ratio of 4:1; (4) a Cu_3P phase with a dark gray color and a Cu:P atomic ratio of 3:1 attached to trigonal grain boundaries or within the δ-$Cu_{41}Sn_{11}$ phase in irregular granular or triangular form (3-point region). Similar results were obtained by Li et al.[32,34,37]

From the EDS of Cu shown in Figure 7(a-1) and (b-1), it is clear that Cu is missing at certain positions, indicating the high-tin brittle intergranular phase (α + δ + Cu_3P). In Figure 7(a-2) and (b-2), there is a gradient in the distribution of Sn, which means that from the primary α-Cu phase to the intergranular phase, the intensity of the Sn distribution gradually increased reaching a maximum at the intergranular phase positions. As shown in Figure 7(a-2), (b-2), and (c-2) that the light-green distribution cloud mapping surrounding the primary α-Cu phase indicates that the Sn was distributed in the form of the $Cu_{13.7}Sn$ phase. Sn was distributed in the form of the δ-Cu41Sn11 phase, represented by the bright-green distribution cloud mapping. Figure 7(c-1) and (c-2) shows that the distributions of Cu and Sn were more uniform at 22mm/s than at low filling speeds. Furthermore, as shown in Figure 7(a-3), (b-3), and (c-3), the distribution of P indicates that P is mainly present as the electronic compound Cu3P and was enriched with the δ-$Cu_{41}Sn_{11}$ phase at the grain boundaries as a reticulate eutectoid. At 22 mm/s, the Sn was more evenly distributed in the form of the $Cu_{13.7}Sn$ phase owing to the decrease in the δ-$Cu_{41}Sn_{11}$ phase content; and P was distributed at the triple junction grain boundaries with the granular or triangular shape.

The line-scan positions shown in Figure 7 (S1, S2, S3, S4, and S5) pass through the four phase regions. As shown in Figure 7, A represents the low-tin primary α-Cu phase region; B is the high-tin solid-solution layer region composed of $Cu_{13.7}Sn$; C is the high-tin δ-$Cu_{41}Sn_{11}$ precipitated brittle and hard phase region, and D is the Cu_3P phase region. As shown in Figure 7(a-4), the strength of Cu decreased slightly, whereas the strength of Sn increased slightly; overall the curve was stable. From Figure 7(a-4) and (b-4), owing to the high-tin brittle δ-$Cu_{41}Sn_{11}$ phase at

the grain boundary, the Cu and Sn element distribution curves underwent a large jump from the A region to the C region or from the C region to the A region. The Cu content decreased sharply, and the Sn content increased significantly, which is why at 18 mm/s and 20 mm/s there is a higher diffraction peak corresponding to δ-$Cu_{41}Sn_{11}$ in the XRD pattern (Figure 6). The line-scan results in Figure 7(c-4) indicate that the strength of Cu was somewhat reduced, and the strength of Sn increased slightly from A to B. As shown in Figure 7(c-4), the B region transitioned into the C region, and the transition amplitudes of the Cu and Sn element distribution curves were greatly reduced. Moreover, from Figure 7(c-2), the aggregation degree of the δ-Cu41Sn11 phase at grain boundaries was greatly reduced, which also explains the noticeable decrease in the corresponding diffraction peaks of δ-$Cu_{41}Sn_{11}$ in the XRD pattern. Comparison of Figure 7(d-2), (e-2), (a-2), and (b-2) shows that the distribution of Sn was more uniform, and there was no clear distribution gradient of Sn. It is essential that the relative concentration of the crystal in the high-tin brittle phase δ-$Cu_{41}Sn_{11}$ phase is considerably reduced, and the Sn appears as $Cu_{13.7}Sn$, as observed in Figure 6. The XRD patterns reveal that the diffraction peak strength of the $Cu_{13.7}Sn$ phase increased with increasing forming specific pressure.

Figure 7(c-3), (d-3), and (e-3) shows that the P distribution was almost completely changed into granular and discretely distributed at the triple junction. From the line-scan results shown in Figure 7(c-4)–(e-4), the amplitude of the Sn distribution curve was significantly lower, with A to C or from C to A, all passing through a wider B region. In other words, from the low-tin primary α-Cu phase region to the high-tin brittle δ-Cu41Sn11 phase region, all must pass through a wider $Cu_{13.7}Sn$ solid-solution layer or a densely distributed spherical $Cu_{13.7}Sn$ phase first, such that there is no large jump in Cu and Sn, as shown in Figure 7(a-4) and (b-4).

Mechanical properties and fracture morphologies

Figure 8a depicts the stress–strain curves for semi-solid rheological squeeze forming of the CuSn10P1 alloy parts with five process parameters, corresponding to the average yield strength (YS), ultimate tensile strength (UTS), and elongation (EL), as shown in Figure 8b. The graphs show that the forming process parameters had a considerable impact on the mechanical properties. The ultimate tensile strength value increased as the filling speeds increased at a forming specific pressure of 145 MPa. The ultimate tensile strength and elongation reached a maximum of 400.30 MPa and 13.32% at 22 mm/s. Similarly, at a filling speed of 22 mm/s, the ultimate tensile strength decreased and subsequently increased as the forming specific pressure increased, reaching a maximum of 419.95 MPa and 13.71% at 165 MPa. Furthermore, at 22 mm/s, the forming
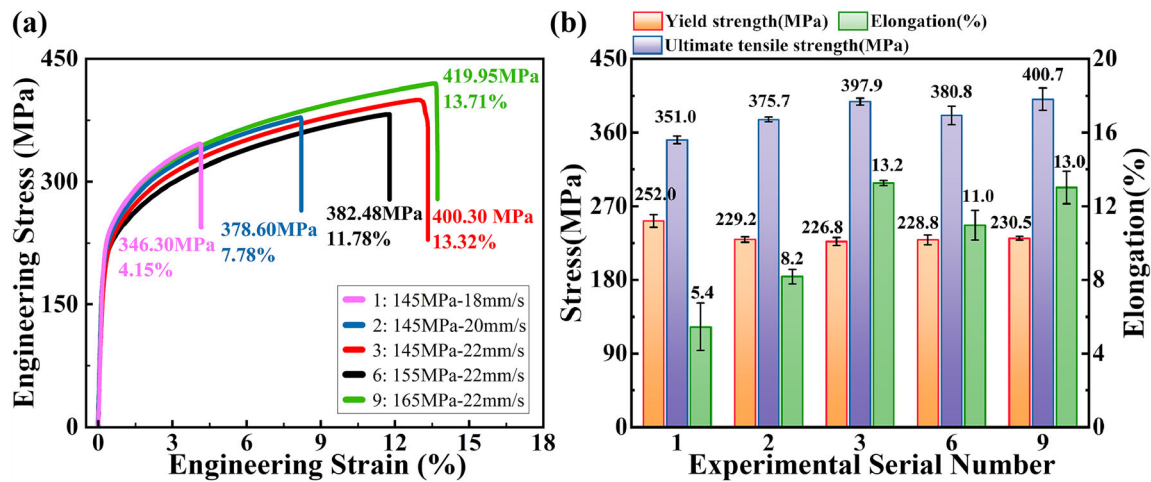
Figure 8. Mechanical properties of CuSn10P1 alloy rheo-squeeze casting parts with different process parameters: (a) stress–strain curves, (b) yield strength, ultimate tensile strength, and elongation.

specific pressures were 145 MPa and 165 MPa, and the parts had similar mechanical properties.

The fracture surface and longitudinal cross section of CuSn10P1 alloy rheologically squeezed parts with different process parameters are shown in Figure 9, using a combination of SEM and OM to determine the fracture type of the CuSn10P1 alloy rheologically squeezed parts during tensile loading.

In Figure 9a, d, for the fracture cross sections in the low magnification SEM images, both fractures had evident holes and large cracks, whereas the tensile fractures all had obvious tough nests at 22 mm/s (Figure 9g, j, m). The fracture surfaces characteristics are enlarged to further investigate their characteristics. As shown in Figure 9b, e, there were large cracks in the parts; the fracture morphology showed typical stone fracture morphology. At 22mm/s, the forming specific pressures were 145 MPa, 155 MPa, and 165 MPa (as shown in Figure 9h, k, n, respectively), Many dense dimples appeared, with average sizes of approximately 5.0 μm, 12.0 μm, and 3.5 μm. When the forming specific pressure is 145 MPa or 165 MPa, there were large dimples (5 μm) and fine dimples closely arranged on the tearing edge. At 155 MPa, some dimples were observed, accompanied by a few small areas of cleavage facets.

The fracture mode was typical of brittle fracture at 145 MPa-18mm/s and 145 MPa-20 mm/s; the tensile strength and elongation were very low; at 155 MPa-22 mm/s, there are tearing ribs, tough dimples, and a small area of cleavage platform at the fracture, a mixed form of quasi-cleavage fracture and ductile fracture. The tensile fractures of the CuSn10P1 alloy parts showed ductile fracture patterns at 145 MPa-22 mm/s and 165 MPa-22

mm/s, indicating that the CuSn10P1 alloy parts exhibited good ductility in these forming conditions.

The crack propagation path was observed using OM images of the longitudinal sections of the interrupted specimens, as shown in Figure 9c, f, i, l. At 145 MPa-18 mm/s and 145 MPa-20 mm/s, cracks propagated along the region of the intergranular high-tin eutectoid phase ($\alpha + \delta + Cu_3P$) (marked with red arrows). Crack sources (marked with magenta arrows) were preferentially generated during external stress-induced deformation because intergranular δ-$Cu_{41}Sn_{11}$ and Cu_3P are hard and brittle phases with low strength, prone to stress concentration, and have weak bonding with the incipient α-Cu matrix. Furthermore, the increased number of crack-generating boundaries made it difficult for dislocations to cross during the plastic deformation of the alloy, resulting in cracking at the phase interface and fracture along the crystal (marked with white arrows). This provides additional evidence that larger size and higher content of intergranular hard and brittle phases have a more severe negative effect on the properties, demonstrating a typical brittle fracture pattern in both processes.

Many incomplete grains (marked with green arrows) were observed at a filling speed of 22 mm/s and forming specific pressure of 145 MPa and 165 MPa, with cracks primarily extending along the inner grain, indicating a grain through fracture pattern. Both processes had hard and brittle intergranular phases that ruptured during unidirectional stretching (marked with magenta arrows). However, due to the low content of brittle intergranular phases, which were not widely distributed and were discrete in the part, even if cracks occurred, they were inhibited by the primary α-Cu phase and the spherical high-Sn $Cu_{13.7}Sn$ phase. Figure 9i, o shows that the spherical or near-spherical grains
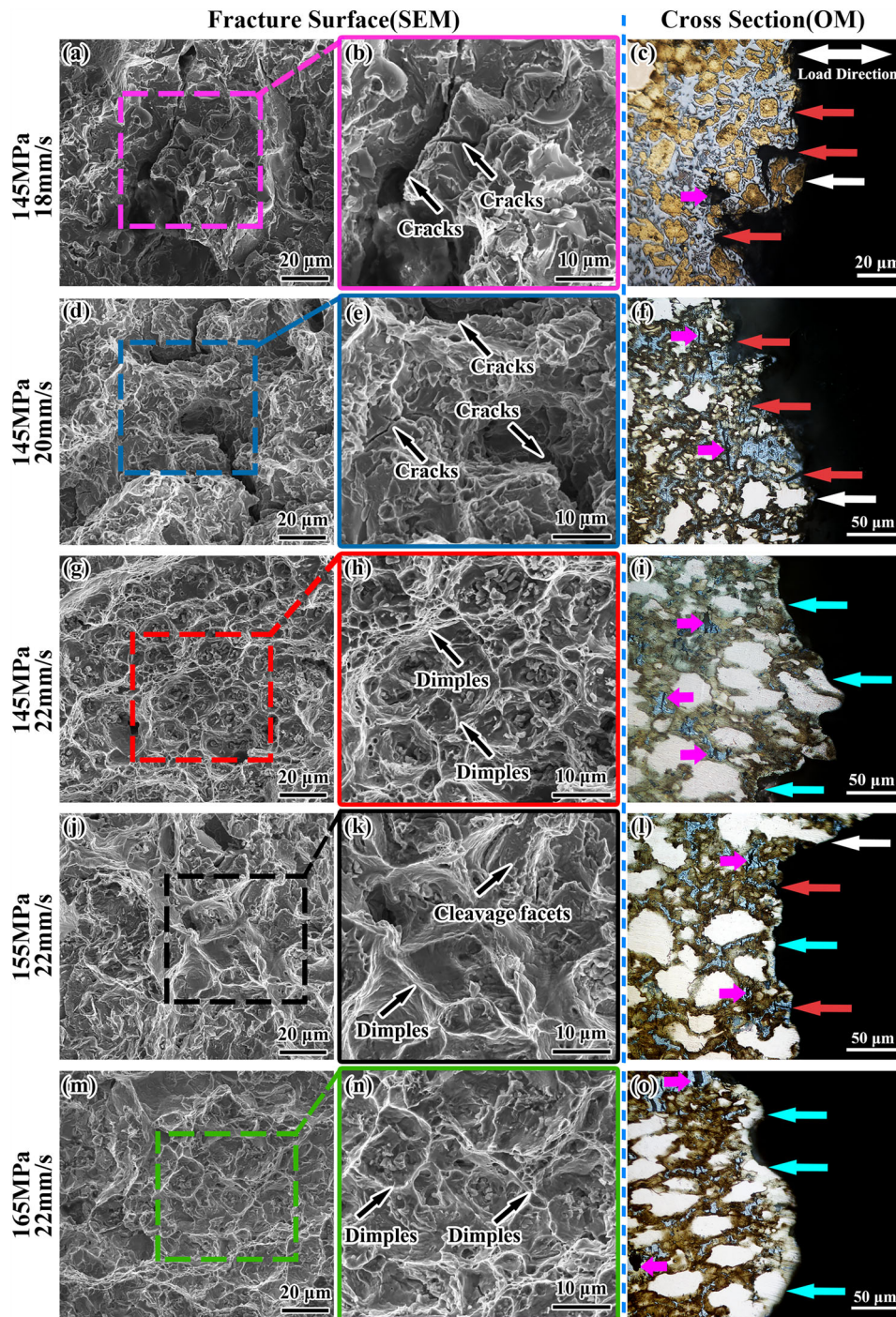
Figure 9. Fracture morphology and longitudinal section of CuSn10P1 alloy rheo-squeeze casting parts with different process parameters.

composed of the primary α-Cu phase and high-tin solid-solution layer, and the $Cu_{13.7}Sn$ phase with a spherical or near-spherical equiaxed shape was clearly elongated, indicating that the performance of parts was fully demonstrated during the large deformation process. This is consistent with the high elongations observed at 145 MPa and 165 MPa.

As shown in Figure 9c, f, the grains remained spherical or nearly spherical, indicating that the part failed due to crack

expansion of the intergranular brittleness before the high strength and high plasticity that the part should possess could be exploited. At a forming specific pressure of 155 MPa, the OM image of the longitudinal section of the tensile fracture was complex. Cracks along the preferential rupture of the intergranular high-tin eutectic phase ($\alpha + \delta + Cu_3P$) with a clear tendency to propagate inward (marked with red arrows) were found, while incomplete grains were observed at the fracture (marked with green arrows). Thus, in process-forming conditions, the crack propagated simultaneously along the high-tin intergranular phase and within the grain, manifesting as both through-grain and along-grain fracture modes.

Discussion

Feasibility Analysis

In this study, thin-walled CuSn10P1 alloy parts with complete filling and good surface quality were successfully fabricated using rheological squeeze casting. The parts exhibited excellent mechanical properties at a filling speed of 22 mm/s and forming specific pressures of 145 MPa and 165 MPa. Although the mechanisms of the superior mechanical properties realized by the two processes were not identical, it was demonstrated that semi-solid rheological squeeze forming on a sheet with a thickness of only 5 mm is completely feasible.

Microstructure Evolution

Optimization of the multi-process parameters of rheological squeeze forming was realized, through an orthogonal experimental design and completion of single-factor and range analyses. Semi-solid rheological squeeze casting was used to produce thin-walled parts made of CuSn10P1 alloy. The composition and type of phase in the part and the distribution and content of the intergranular phase ($\alpha + \delta + Cu_3P$), which plays an important role in the overall mechanical properties, are directly affected by the extrusion process parameters. Consequently, the forming
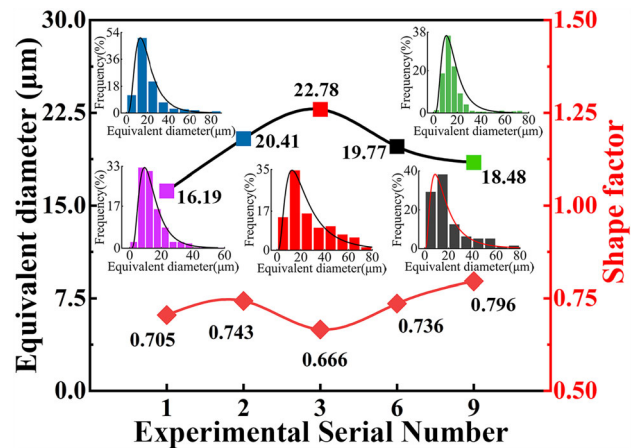
Figure 11. Average grain size and shape factor of solid grains of CuSn10P1 parts formed with different process parameters.
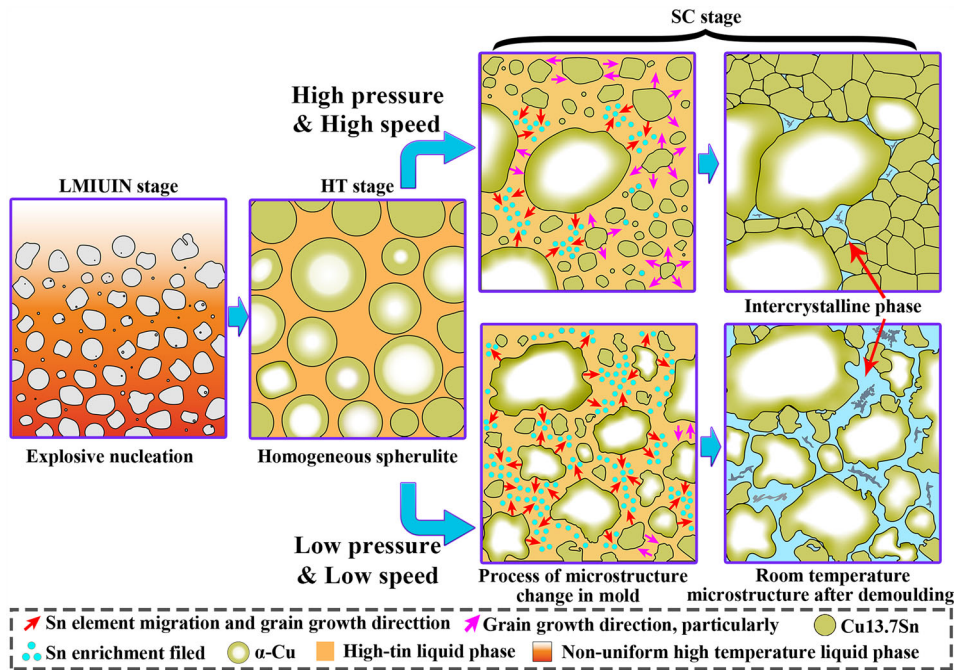
Figure 10. Microstructure evolution diagram of CuSn10P1 alloy from semi-solid slurry preparation to rheo-squeeze casting.

specific pressure (MPa) and filling speed (mm/s) significantly affect the mechanical properties of the parts.

Figure 10 depicts the evolution of the microstructure of the CuSn10P1 alloy from semi-solid slurry preparation through the rheological squeeze-forming process. The microstructural evolution was divided into three stages:[32–35]

(1) In the first stage, using the liquid-metal instantaneous undercooling-induced nucleation (LMIUIN stage) to prepare CuSn10P1 alloy semi-solid slurry (Figures 1c, 10), the melt can be cooled at an extremely high cooling rate (approximately 450 °C/s) for a short time.[16] The strong cooling forces the melt to undergo explosive nucleation, with the primary α-Cu phase growing in a spherical or subspherical manner while expelling Sn elements into the remaining liquid phase,[30,32,36] resulting in the formation of the CuSn10P1 semi-solid slurry in a collection crucible, with many inhomogeneous sizes and shapes of primary α-Cu phases and inhomogeneous Sn content in the liquid phase.

(2) In the second stage, after homogenization treatment (HT stage) (Figures 1d, 11), further solute concentration fluctuations in the liquid phase were eliminated; local aggregation of Sn was avoided to a certain extent, and Sn diffusion from the α-Cu phase to the intercrystalline phase was inhibited, achieving microstructure homogenization.[5,32,38] A semi-solid slurry consisting of a spherical primary α-Cu phase with a high-Sn solid solubility of approximately 13.7% on the outer wall and a high-Sn liquid phase with uniform Sn content was generated after a short (20 ± 0.5 s) homogenization treatment.

(3) As shown in Figures 1e, 11, in the semi-solid rheological squeeze-casting stage (SC stage), after the semi-solid slurry was injected into the extruder barrel, there were two scenarios depending on the forming specific pressure and filling speed:

(1) With low filling speed and forming specific pressure conditions, after the homogenization treatment stage, the secondary nucleated grains in the mold barrel entered the mold cavity together with the spherical primary α-Cu phase wrapped in the high-tin solid-solution ring. The grains had a long enough time to grow and continuously discharge Sn to the front of the solid–liquid interface. Moreover, the primary α-Cu phase was extruded and deformed under the action of squeezing pressure, causing some of the grains to become entangled, resulting in the irregular grain shape, facilitating grain growth in a specific direction and Sn accumulation in a specific orientation. Similar results were reported by He.[33] In addition, the average equivalent diameter of the grains was the smallest, as shown in Figures 4a, 11, at 145 MPa-18 mm/s, because the remaining high-tin liquid phase was secondarily nucleated on the barrel wall and in the mold cavity to form a portion of the

spherical or near-spherical $Cu_{13.7}Sn$ phase. Due to the slow filling speed and low forming specific pressure, the spherical $Cu_{13.7}Sn$ phase of the secondary nucleation solidified before it had grown sufficiently to consume a significant amount of Sn from the remaining high-Sn liquid phase, resulting in the largest volume fraction of this part of the intergranular phase ($\alpha + \delta + Cu_3P$).

(2) In high filling speed and forming specific pressure conditions, the high forming specific pressure of the punch on the semi-solid slurry in the barrel reduces the nucleation radius, promoting heterogeneous nucleation[32] and forcing the remaining high-tin liquid phase to nucleate more readily in the barrel and mold cavity in the secondary form. More nucleation means that more Sn in the liquid phase can be consumed, resulting in the α-Cu phase with a high-tin solid-solution ring. The faster filling speed ensured that the semi-solid CuSn10P1 alloy slurry reached the mold cavity faster. This prevented a large accumulation of Sn at the grain boundaries after the solid-solution level had reached its limit (13.5%); reaching the mold cavity faster allow solidification at nearly the same cooling rate, avoiding the bias of Sn at the grain boundaries caused by different cooling rates. The combined effect of these two factors allowed the primary α-Cu phase to grow with the spherical high-tin $Cu_{13.7}Sn$ phase during the nucleation process. The Sn element in the solid–liquid interface front was not enriched in a specific growth direction; thus, the composition of Sn throughout the cooling process did not meet the conditions for the formation of an inclusion-like β phase, ultimately resulting in a lower δ-$Cu_{41}Sn_{11}$ phase content in the part. Ultimately, the δ-$Cu_{41}Sn_{11}$ phase in the part was much lower and the Sn was present in the part as a spherical high-tin $Cu_{13.7}Sn$ phase before it diffused from the intracrystalline to the intergranular. This explains why, for the nine process parameters shown in Figure 4, the higher the forming specific pressure and filling speed, the higher the relative content of the spherical or nearly spherical dark-brown Cu13.7Sn phase in the microstructure of the part, and the significant increase in the intensity of the corresponding Cu13.7Sn diffraction peak (Figure 6). Similar conclusions were reached by Chakkravarthy et al.[39,40] in their studies on semi-solid squeeze-forming processes for other alloys.

Strengthening Mechanisms

Figure 10 depicts the equivalent diameter and shape factor distribution of the grains at 145 MPa-18 mm/s, 145 MPa-20 mm/s, 145 MPa-22 mm/s, 155 MPa-22mm/s and 165 MPa-22 mm/s (corresponding to experiment numbers 1, 2, 3, 6, and 9, respectively) (the equivalent diameter refers to the solid particles in the room-temperature microstructure, except for the intergranular phase). Figure 11 shows that the average equivalent diameter of the grains increased in a regular upward trend with an increase in filling speed at a

forming pressure of 145 MPa, and decreased in a more uniform trend with increasing filling pressure at a filling speed of 22 mm/s.[16,33]

Semi-solid CuSn10P1 alloy is now commonly strengthened in three ways: fine-grain strengthening, solid-solution strengthening, and microstructural homogenization.[32,33] The fine-grain strengthening mechanism is primarily characterized by a reduction in grain size, an increase in the number of grain boundaries per unit area, and an increase in the barrier effect of the grain boundaries on dislocation movement, resulting in an increase in the tensile strength.[41] The fine-grain strengthening due to the average grain refinement in this study can be expressed using the Hall–Petch equation[42] :

$$\Delta\sigma_{HP} = K_{HP} \cdot d^{-1/2}$$

In the equation $K_{HP} = 4.5$ MPa mm$^{1/2}$,[33] d is the average grain size. Fine-grain strengthening contributes 35.37 MPa, 31.50 MPa, 29.82 MPa, 32.00 MPa, and 33.11 MPa to the strength values in the parts, respectively. The difference in strength provided by fine-grained strengthening was not obvious; the maximum difference was 5.56 MPa. According to Figure 11, the average grain size was 16.19 μm when the forming specific pressure was 145 MPa and the filling speed was 18mm/s. Although the average equivalent diameter of the grain was larger than with 145 MPa-22 mm/s, the average ultimate tensile strength is 397.9 MPa and 13.20%, much higher than 351.0 MPa and 5.1%, respectively, with 145 MPa and 18 mm/s. As a result, fine-grain strengthening cannot be regarded as the sole cause of the change in strength and plasticity of the CuSn10P1 alloy semi-solid rheo-squeeze casting parts. Three scenarios can be considered:

(1) At 145 MPa-18 mm/s and 145 MPa-20 mm/s, the intergranular phase content was high; it nearly completely wrapped the Cu$_{13.7}$Sn phase and primary α-Cu phase, forcing them to be isolated by the intergranular phases, even if the grain size was relatively small for these two process parameters. This is because the intergranular δ-Cu$_{41}$Sn$_{11}$ and Cu$_3$P brittle phases disrupted the continuity and homogeneity of the microstructure, resulting in stress concentration;[9] high strength and elongation could not be fully reflected in the brittle intergranular phase, causing the brittle fracture. The ultimate tensile strength was limited to 329.3–378.6 MPa, and elongation was limited to 4.15–8.56%.

(2) At 145 MPa-18 mm/s and 145 MPa-20 mm/s, the line-scan results in Figure 7 and point-scan results in Figure 7f show a significant increase in the solid solution of Sn in the primary α-Cu phase and a decrease in the content of the intergranular phase, respectively. The microstructure homogeneity was improved, and the ultimate tensile strength and elongation were increased to some extent, as
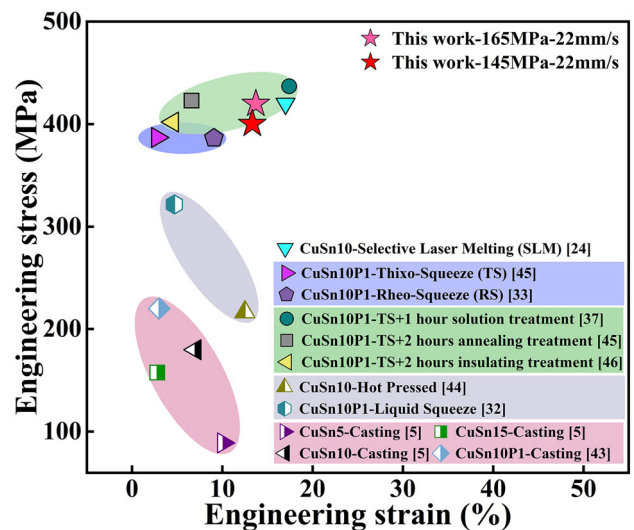

Figure 12. Comparison of mechanical properties with different forming processes.

shown in Figure 7. The ultimate tensile strength remained at 382.48–401.40 MPa and the elongation remained at 10.15–13.37%. A primary reason for the high strength and plasticity of parts is microstructural uniformity. He[33] and Li[32] reached similar conclusions in their studies.

(3) It was discovered that the intercrystalline phase content was 2.57% higher at 165 MPa-22 mm/s than at 145 MPa-22 mm/s. From the results, lower ultimate tensile strength and elongation than at 145 MPa - 22 mm/s were expected. However, the mechanical properties were essentially the same as those with 145 MPa-22 mm/s (Figure 8a). Furthermore, the diffraction peak intensity of Cu$_{13.7}$Sn at 165 MPa-22 mm/s was significantly higher than that at 145 MPa-22 mm/s, according to the XRD results. Comparing Figure 4c, f, it is clear that the microstructures of the parts differ significantly. The Cu$_{13.7}$Sn phase was mainly wrapped outside the primary α-Cu phase in the form of a dark-brown annular high-tin solid-solution ring, as shown in Figure 4c, which is consistent with our previous results.[32–35] However, as shown in Figure 4f, the Cu$_{13.7}$Sn phase was present not only as a high-tin solid-solution ring but also as a large number of equiaxed fine dark-brown spherical Cu$_{13.7}$Sn phases surrounding the primary α-Cu phase. It can be concluded that while both process parameters provide excellent mechanical properties, the strengthening mechanisms are not identical. The different strengthening mechanisms of the two process parameters can be classified as follows:

(1) At 145 MPa-22 mm/s, the content of the high-tin intergranular phase decreased as the Sn migrated from the grain boundary to the primary α-Cu phase; the microstructure was primarily laminated and wrapped around the primary α-Cu phase to form a spherical or nearly spherical grain shape. The high strength and

plasticity can be attributed primarily to solid-solution strengthening.

(2) At 165 MPa-22 mm/s, there was a large amount of new spherical high-tin $Cu_{13.7}Sn$ phase in addition to the $Cu_{13.7}Sn$ phase in the form of high-tin solid-solution rings, which led to a decrease in the content of δ-$Cu_{41}Sn_{11}$ phase as the $Cu_{13.7}Sn$ phase increased, proving that the solid-solution strengthening mechanism was a main strengthening mechanism. In addition, the dispersion of a diffusely distributed $Cu_{13.7}Sn$ phase in the form of spheres ensured that even if a small amount of the brittle intergranular phase was cracked by unidirectional tensile action, the increase in the number of grain boundaries per unit area caused by the fine-grain strengthening mechanism effectively inhibited the expansion of microcracks (Figure 9o), ensuring the high strength and plasticity of the part. Owing to the synergy between these two mechanisms, the parts produced in these process conditions had high strength and plasticity.

Microstructural homogeneity and solid-solution strengthening are common strengthening mechanisms for CuSn10P1 alloy semi-solid rheological squeeze-casting parts. When the $Cu_{13.7}Sn$ phase was present in the microstructure as spherical equiaxed crystals after process optimization, the contribution of the fine-grain strengthening mechanism to the increase in plasticity is not negligible. The overall mechanical properties of the part can be improved if the forming process parameters are further optimized such that the main phases of the part contain only primary α-Cu and $Cu_{13.7}Sn$ phases.

The mechanical properties of parts formed using conventional methods were compared to highlight the superiority of the CuSn10P1 alloy rheological squeeze-cast parts in this study, as shown in Figure 12. The ultimate tensile strength of the CuSn10P1 rheo-squeezed parts produced using the process in this paper was significantly higher than that of conventionally cast parts,[5,43] parts produced using liquid squeeze,[32] and parts produced through hot-pressed processing,[44] higher than that of heat-treated CuSn10P1 alloy thixotropic parts,[37,45,46] but slightly lower than that of parts produced with selective laser melting.[24]

Conclusion

CuSn10P1 alloy rheological squeeze-casting parts with complete filling and good surface quality were successfully and stably prepared using casting methods The main conclusions are presented as follows.

(1) During the formation stage, filling speed (mm/s) significantly affected the elongation (%) of CuSn10P1. The best process parameters for forming CuSn10P1 alloy by rheological squeeze

casting are [165 MPa, 22 mm/s, 485 °C]. Parts formed in these conditions have good overall mechanical properties (UTS of 419.95 MPa, EL of 13.71%).

(2) Semi-solid rheological squeeze casting of CuSn10P1 alloy is feasible for thin-walled parts; the mechanical properties are directly related to the content of intergranular brittle phases ($\alpha + \delta + Cu_3P$), with ultimate tensile strength (MPa) and elongation (%) showing a significant and consistent decrease with an increase in intergranular brittle phases.

(3) At 165 MPa-22 mm/s, the $Cu_{13.7}Sn$ phase was found in two forms: as a high-tin solid-solution circle, as in our previous study, and as a spherical or nearly spherical form distributed around the low-tin primary α-Cu phase.

(4) The mechanical properties of parts fabricated at 165 MPa-22 mm/s were similar to those at 145 MPa-22 mm/s, but the strengthening mechanisms were different; 145 MPa-22 mm/s indicated solid-solution strengthening and microstructural homogeneity. In contrast, at 165 MPa-22 mm/s, in addition to solid-solution strengthening and microstructural homogeneity, fine-grain strengthening significantly improved the plasticity of the parts.

To determine the optimum semi-solid forming parameters, the influence of other forming parameters such as holding time, pressure retention time, and mold temperature will be investigated in further research.

REFERENCES

1. J.S. Park, C.W. Park, K.J. Lee, Implication of peritectic composition in historical high-tin bronze metallurgy. Mater. Charact. **60**, 1268–1275 (2009). https://doi.org/10.1016/j.matchar.2009.05.009

2. S. Jie, M. Ting-yun, Q. Hui-xuan, L. Qi-song, Electrochemical behaviors and electrodeposition of single-phase Cu–Sn alloy coating in [BMIM]Cl. Electrochim. Acta **297**, 87–93 (2019). https://doi.org/10.1016/j.electacta.2018.11.189

3. Y. Liu, L. Wang, K. Jiang, S. Yang, Electro-deposition preparation of self-standing Cu–Sn alloy anode electrode for lithium ion battery. J. Alloys Compd. **775**,

818–825 (2019). https://doi.org/10.1016/j.jallcom.2018.10.207

4. J.B. Singh, W. Cai, P. Bellon, Dry sliding of Cu–15 wt%Ni–8 wt%Sn bronze: wear behaviour and microstructures. Wear **263**, 830–841 (2007). https://doi.org/10.1016/j.wear.2007.01.061

5. S.M. So, K.Y. Kim, S.J. Lee, Y.J. Yu, H.A. Lim, M.S. Oh, Effects of Sn content and hot deformation on microstructure and mechanical properties of binary high Sn content Cu–Sn alloys. Mater. Sci. Eng. A (2020). https://doi.org/10.1016/j.msea.2020.140054

6. M.C. Flemings, Behavior of metal alloys in the semisolid state. Metall. Trans. A **22**, 957–981 (1991). https://doi.org/10.1007/BF02661090

7. A. Rassili, M. Robelet, R. Bigot, Thixoforming of steel: parameters and means for industrialization. Solid State Phenom. **141**, 213–218 (2008). https://doi.org/10.4028/www.scientific.net/SSP.141-143.213

8. K.N. Campo, C.C. de Freitas, S.-C. Moon, R. Dippenaar, R. Caram, In-situ microstructural observation of Ti–Cu alloys for semi-solid processing. Mater. Charact. **145**, 10–19 (2018). https://doi.org/10.1016/j.matchar.2018.08.016

9. M. Kiuchi, R. Kopp, Mushy/semi-solid metal forming technology—present and future. CIRP Ann. **51**, 653–670 (2002). https://doi.org/10.1016/s0007-8506(07)61705-3

10. J. Mathew, A. Mandal, S.D. Kumar, S. Bajpai, M. Chakraborty, G.D. West, P. Srirangam, Effect of semi-solid forging on microstructure and mechanical properties of in-situ cast Al–Cu–TiB$_2$ composites. J. Alloys Compd. **712**, 460–467 (2017). https://doi.org/10.1016/j.jallcom.2017.04.113

11. M.R. Rokni, A. Zarei-Hanzaki, H.R. Abedi, N. Haghdadi, Microstructure evolution and mechanical properties of backward thixoextruded 7075 aluminum alloy. Mater. Des. **1980–2015**(36), 557–563 (2012). https://doi.org/10.1016/j.matdes.2011.11.061

12. H.R. Abedi, A. Zarei-Hanzaki, S.M. Fatemi-Varzaneh, A.A. Roostaei, The semi-solid tensile deformation behavior of wrought AZ31 magnesium alloy. Mater. Des. **31**, 4386–4391 (2010). https://doi.org/10.1016/j.matdes.2010.05.004

13. S. Lü, S. Wu, X. Yang, L. Hao, W. Guo, X. Fang, Microstructure and mechanical properties of Mg$_{97}$Zn$_1$Y$_2$ alloy reinforced with LPSO structure produced by semisolid squeeze casting. Mater. Sci. Eng. A **732**, 359–367 (2018). https://doi.org/10.1016/j.msea.2018.07.025

14. Q.Y. Pan, S. Wiesner, D. Apelian, Application of the continuous rheoconversion process (CRP) to low temperature HPDC-part I: microstructure. Solid State Phenom. **116**, 402–405 (2006). https://doi.org/10.4028/www.scientific.net/SSP.116-117.402

15. Q. Pan, M. Findon, D. Apelian, The continuous rheoconversion process (CRP): a novel SSM approach. In: 8th International Conference on Semi-Solid Processing of Alloys and Composites (2004).

16. G. Xiao, J. Jiang, Y. Wang, Y. Liu, Y. Zhang, Microstructure and mechanical properties of nickel-based superalloy GH4037 parts formed by thixo-forming. Mater. Sci. Eng. A (2020). https://doi.org/10.1016/j.msea.2020.139196

17. Y. Meng, S. Sugiyama, J. Yanagimoto, Microstructural evolution during RAP process and deformation behavior of semi-solid SKD61 tool steel. J. Mater. Process. Technol. **212**, 1731–1741 (2012). https://doi.org/10.1016/j.jmatprotec.2012.04.003

18. Y. Meng, S. Sugiyama, M. Soltanpour, J. Yanagimoto, Effects of predeformation and semi-solid processing on microstructure and mechanical properties of Cr–V–Mo steel. J. Mater. Process. Technol. **213**, 426–433 (2013). https://doi.org/10.1016/j.jmatprotec.2012.09.021

19. J. Jiang, G. Xiao, Y. Wang, Y. Qi, Microstructure evolution of wrought nickel based superalloy GH4037 in the semi-solid state. Mater. Charact. **141**, 229–237 (2018). https://doi.org/10.1016/j.matchar.2018.04.057

20. M. Cao, Z. Wang, Q. Zhang, Microstructure-dependent mechanical properties of semi-solid copper alloys. J. Alloys Compd. **715**, 413–420 (2017). https://doi.org/10.1016/j.jallcom.2017.03.360

21. L. Jia, X. Lin, H. Xie, Z.-L. Lu, X. Wang, Abnormal improvement on electrical conductivity of Cu–Ni–Si alloys resulting from semi-solid isothermal treatment. Mater. Lett. **77**, 107–109 (2012). https://doi.org/10.1016/j.matlet.2012.03.010

22. G. Xiao, J. Jiang, Y. Wang, Y. Liu, Y. Zhang, Effects of forming temperature, soaking time and dwell time on the microstructure and mechanical properties of thixoformed nickel-based superalloy parts. J. Mater. Res. Technol. JMRT **10**, 1250–1261 (2021). https://doi.org/10.1016/j.jmrt.2020.12.111

23. Z.F. Huang, J.D. Xing, C. Guo, Microstructure and properties of semisolid hypereutectic high chromium cast iron prepared by slope cooling body method. Ironmak. Steelmak. **37**, 607–611 (2013). https://doi.org/10.1179/030192309x12549935902266

24. S. Scudino, C. Unterdörfer, K.G. Prashanth, H. Attar, N. Ellendt, V. Uhlenwinkel, J. Eckert, Additive manufacturing of Cu–10Sn bronze. Mater. Lett. **156**, 202–204 (2015). https://doi.org/10.1016/j.matlet.2015.05.076

25. P. Han, F. Xiao, W. Zou, B. Liao, Influence of hot pressing temperature on the microstructure and mechanical properties of 75% Cu–25% Sn alloy. Mater. Des. **53**, 38–42 (2014). https://doi.org/10.1016/j.matdes.2013.06.024

26. Z. Mao, D.Z. Zhang, J. Jiang, G. Fu, P. Zhang, Processing optimisation, mechanical properties and microstructural evolution during selective laser melting of Cu–15Sn high-tin bronze. Mater. Sci. Eng. A

721, 125–134 (2018). https://doi.org/10.1016/j.msea.2018.02.051

27. E. Erzi, M. Tiryakioğlu, Feeding distance of tin bronze castings: intrinsic and extrinsic estimates. Mater. Sci. Technol. **35**, 2211–2216 (2019). https://doi.org/10.1080/02670836.2019.1666226

28. X. Liu, J. Luo, X. Wang, L. Wang, J. Xie, Columnar grains-covered small grains Cu–Sn alloy prepared by two-phase zone continuous casting. Prog. Nat. Sci. Mater. Int. **23**, 94–101 (2013). https://doi.org/10.1016/j.pnsc.2013.01.014

29. A.P. Ventura, C.A. Wade, G. Pawlikowski, M. Bayes, M. Watanabe, W.Z. Misiolek, Mechanical properties and microstructural characterization of Cu-4.3 Pct Sn fabricated by selective laser melting. Metall. Mater. Trans. A-Phys. Metall. Mater. Sci. **48**, 178–187 (2016). https://doi.org/10.1007/s11661-016-3779-x

30. J.Y. Yang, G.H. Kim, W.J. Kim, High-strain-rate solute drag creep in a Cu-22%Sn alloy ($Cu_{17}Sn_3$) with near peritectic composition. Mater. Charact. (2020). https://doi.org/10.1016/j.matchar.2020.110325

31. B.B. Straumal, A.R. Kilmametov, B. Baretzky, O.A. Kogtenkova, P.B. Straumal, L. Lityńska-Dobrzyńska, R. Chulist, A. Korneva, P. Zięba, High pressure torsion of Cu–Ag and Cu–Sn alloys: limits for solubility and dissolution. Acta Mater. **195**, 184–198 (2020). https://doi.org/10.1016/j.actamat.2020.05.055

32. Y. Li, L. Li, B. Geng, Q. Wang, R. Zhou, X. Wu, H. Xiao, Microstructure characteristics and strengthening mechanism of semisolid CuSn10P1 alloys. Mater. Charact. (2021). https://doi.org/10.1016/j.matchar.2021.110898

33. Z. He, R. Zhou, Y. Li, T. Liu, W. Xiong, Z. Liu, C. Wang, H. Xiao, Effect of wall thickness on microstructure uniformity and properties of CuSn10P1 alloy in semi-solid rheological squeeze casting. Rare Metal Mat. Eng. **51**, 4157–4165 (2022)

34. Z. Liu, R. Zhou, W. Xiong, Z. He, T. Liu, Y. Li, Compressive rheological behavior and microstructure evolution of a semi-solid CuSn10P1 alloy at medium temperature and low strain. Metals (2022). https://doi.org/10.3390/met12010143

35. W. Xiong, R. Zhou, Z. Liu, Y. Li, Research on neural network genetic algorithm optimization in the preparation of CuSn10P1 semi-solid slurry with the fully enclosed melt-constrained cooling inclined plate. J. Adv. Mech. Des. Syst. Manuf. (2021). https://doi.org/10.1299/jamdsm.2021jamdsm0026

36. Q. Wang, R. Zhou, Y. Li, B. Geng, Characteristics of dynamic recrystallization in semi-solid CuSn10P1 alloy during hot deformation. Mater. Charact. (2020). https://doi.org/10.1016/j.matchar.2019.109996

37. Y. Zhou, Y. Cui, Q. Zhang, Z. Yang, Y. Li, H. Xiao, Effect of solution temperature on microstructure and properties of thixotropic back-extruded tin-bronze shaft sleeve. Materials (Basel) (2022). https://doi.org/10.3390/ma15155254

38. P. Das, P. Dutta, Phase field modelling of microstructure evolution and ripening driven grain growth during cooling slope processing of A356 Al alloy. Comput. Mater. Sci. **125**, 8–19 (2016). https://doi.org/10.1016/j.commatsci.2016.08.022

39. V. Chakkravarthy, M. Lakshmanan, P. Manojkumar, R. Prabhakaran, Crystallographic orientation and wear characteristics of TiN, SiC, Nb embedded Al7075 composite. Mater. Lett. (2022). https://doi.org/10.1016/j.matlet.2021.130936

40. C. Wang, Z. Dong, K. Li, M. Sun, J. Wu, K. Wang, G. Wu, W. Ding, A novel process for grain refinement of Mg–RE alloys by low frequency electro-magnetic stirring assisted near-liquidus squeeze casting. J. Mater. Process. Technol. (2022). https://doi.org/10.1016/j.jmatprotec.2022.117537

41. Y. Yang, P. Tan, Y. Sui, Y. Jiang, R. Zhou, Influence of Zr content on microstructure and mechanical properties of As-cast Al–Zn–Mg–Cu alloy. J. Alloys Compd. (2021). https://doi.org/10.1016/j.jallcom.2021.158920

42. D.V. Kudashov, H. Baum, U. Martin, M. Heilmaier, H. Oettel, Microstructure and room temperature hardening of ultra-fine-grained oxide-dispersion strengthened copper prepared by cryomilling. Mater. Sci. Eng. A **387–389**, 768–771 (2004). https://doi.org/10.1016/j.msea.2004.05.049

43. H. Xiao, Z. Duan, N. Li, Y. Li, R. Zhou, D. Lu, Y. Jiang, Mechanical properties of thixo-extruded copper alloy. Rare Metal Mat. Eng. **48**, 531–537 (2019)

44. A.E. Nassef, A.I. Alateyah, M.A. El-Hadek, W.H. El-Garaihy, Mechanical behavior and fracture surface characterization of liquid-phase sintered Cu–Sn powder alloys. Adv. Mater. Lett. **8**, 717–722 (2017). https://doi.org/10.5185/amlett.2017.1485

45. H. Xiao, Y. Cui, C. Xiong, L. Chen, X. Zhang, Y. Li, R. Zhou, Effect of annealing temperature on microstructure and properties of thixo-extruded tin bronze bushing. Rare Metal Mat. Eng. **50**, 4119–4127 (2021)

46. H. Xiao, Z. Duan, N. Li, C. Xiong, R. Zhou, D. Lu, Y. Jiang, Effect of heat treatment temperature on microstructure and mechanical properties of semi-solid extruded tin bronze. Rare Metal Mat. Eng. **48**, 235–241 (2019)